Journal of Alloys and Compounds 509 (2011) 5326–5335

Contents lists available at ScienceDirect

Journal of Alloys and Compounds

journal homepage: www.elsevier.com/locate/jallcom

Structure, ferroelectric/magnetoelectric properties and leakage current density of $(Bi_{0.85}Nd_{0.15})FeO_3$ thin films

A.Z. Simões [a], L.S. Cavalcante [b,*], F. Moura [c], E. Longo [b], J.A. Varela [b]

[a] Universidade Estadual Paulista, Faculdade de Engenharia de Guaratinguetá, P.O. Box 333, 12516-410 SP, Brazil
[b] Universidade Estadual Paulista, P.O. Box 355, 14801-907 Araraquara, SP, Brazil
[c] UNIFEI–Universidade Federal de Itajubá-Campus Itabira, Rua São Paulo, P.O. Box 377, 35900-37 Itabira, MG, Brazil

ARTICLE INFO

Article history:
Received 13 October 2010
Received in revised form 2 February 2011
Accepted 4 February 2011
Available online 12 February 2011

Keywords:
Ferroelectrics
Chemical synthesis
Piezoelectricity
Magnetic measurements

ABSTRACT

In this paper, we report on the structure, ferroelectric/magnetoelectric properties and improvement of leakage current density of $(Bi_{0.85}Nd_{0.15})FeO_3$ (BNFO) thin films deposited on Pt(1 1 1)/Ti/SiO_2/Si substrates from the polymeric precursor method. X-ray patterns and Rietveld refinement indicated that BNFO thin films with a tetragonal structure can be obtained at 500 °C for 2 h in static air. Field emission scanning electron, atomic force and piezoelectric force microscopies showed the microstructure, thickness and domains with polarization-oriented vectors of BNFO thin films. Ferroelectric and magnetoelectric properties are evident by hysteresis loops. The magnetoelectric coefficient measurement was performed to show the magnetoelectric coupling behavior. The maximum magnetoelectric coefficient in the longitudinal direction was close to 12 V/cm Oe. Piezoresponse force microscopy micrographs reveal a polarization reversal with 71° and 180° domain switchings and one striped-domain pattern oriented at 45° besides the presence of some nanodomains with rhombohedral phase involved in a matrix with tetragonal structure. The cluster models illustrated the unipolar strain behavior of BNFO thin films. The leakage current density at 5.0 V is equal to 1.5×10^{-10} A/cm^2 and the dominant mechanism in the low-leakage current for BNFO thin films was space-charge-limited conduction.

© 2011 Elsevier B.V. All rights reserved.

1. Introduction

In recent years, multiferroic materials have attracted much attention in the scientific community due to the possibility of manipulating the magnetic state by an electric field or vice versa [1]. Researchers have reported [2,3] that the composite materials (yttrium iron garnet/lead magnesium niobate-lead titanate and barium titanate/cobalt ferrite) present separate piezoelectric and magnetic phases with magnetoelectric coupling at room temperature. In addition, the preparation of these composite materials is very difficult and few magnetoelectric multiferroics materials at room temperature have been reported so far [4].

Among multiferroic materials, bismuth ferrite ($BiFeO_3$) has been extensively investigated in the form of ceramics, crystals, nanopowders and thin films [5–12] due to its superior magnetic, visible-light photocatalytic, photoconductive and ferroelectric properties and high ferroelectric polarization with a ferroelectric Curie temperature (T_C) of 820 °C and an antiferromagnetic Néel temperature (T_N) of 370 °C [13,14]. Both ferroelectricity and antiferromagnetism have long been known in $BiFeO_3$ single crystals [15–18]. Recently, several experimental papers reported the existence of a large ferroelectric polarization as well as a small magnetization in doped $BiFeO_3$ [19–21]. However, one of the major drawbacks related to $BiFeO_3$ is its high leakage current density. Therefore, it allows current to pass through when a high voltage is applied [22–24]. Currently, great efforts have been made to improve electrical properties by doping with rare-earth elements such as: lanthanum [25–29], praseodymium [30,31], samarium [32–35], europium [36–39], gadolinium [40,41], dysprosium [42,43] and neodymium (Nd) [44–48]. Among these rare-earth elements, the employment of Nd as a dopant in $BiFeO_3$ thin films/ceramics has shown an improvement in ferroelectric and ferromagnetic properties [49,50].

Thus, in this paper, we report on the structural refine, ferroelectric/magnetoelectric properties and leakage current density of $(Bi_{0.85}Nd_{0.15})FeO_3$ (BNFO) thin films prepared by the polymeric precursor method and grown on Pt(1 1 1)/Ti/SiO_2/Si substrates after heat treatment at 500 °C for 2 h in static air. These films were characterized by X-ray diffraction (XRD), field emission scanning electron microscopy (FE-SEM), atomic force microscopy (AFM) and piezoelectric force microscopy (PFM). The electrical properties were investigated by polarization/magnetic hysteresis loops, strain response, magnetic electric coefficients and improvement of leakage current density.

* Corresponding author. Tel.: +55 16 3361 5215; fax: +55 16 3351 8214; mobile: +55 16 8149 8182.
E-mail address: laeciosc@bol.com.br (L.S. Cavalcante).

0925-8388/$ – see front matter © 2011 Elsevier B.V. All rights reserved.
doi:10.1016/j.jallcom.2011.02.030

2. Experimental details

BNFO thin films were prepared by the polymeric precursor method, as described elsewhere [51]. Phase analysis by Rietveld routine of the films was performed at room temperature by X-ray diffraction (XRD) patterns recorded on a (Rigaku-DMax 2000PC) with Cu Kα radiation in the 2θ range from 20 to 60° with 0.02°/min. The electrical properties of the Pt/BNFO/Pt/Ti/SiO_2/Si(1 0 0) capacitor structure were measured. The upper electrodes of Pt for the electrical measurements were prepared by evaporation through a shadow mask with a 0.2 mm^2 dot area. Dielectric spectroscopy measurements were taken with a frequency response analyzer (Agilent HP model 4294A) at frequencies ranging from 40 Hz to 110 MHz with an amplitude voltage of 1 V. The hysteresis loop measurements were carried out on the films with a Radiant Technology RT6000HVS at a measured frequency of 60 Hz. These loops were traced using the Charge 5.0 program included in the software of the RT6000HVS in a virtual ground mode test device. Magnetoelectric coefficient measurements in BNFO films were attained by a dynamic lock-in technique. The *dc* magnetic bias field was produced by an electromagnet (Cenco Instruments *J*-type). The time-varying *dc* field was achieved by a programmable *dc* power supply (Phillips PM2810 60 V/5 A/60 W). To measure the *dc* magnetic field, a Hall probe was employed. Magnetization measurements were done by using a Vibrating Sample Magnetometer (VSM) from Quantum Design™. The magnetoelectric signal was measured by using a lock-in amplifier (EG & G model 5210) with an input resistance and capacitance of 100 MΩ and 25 pF, respectively. The microstructure and thickness of the annealed films was measured using FE-SEM of Carl Zeiss, model Supra 35-VP (Germany), operated at 6 kV. Piezoelectric measurements were carried out using a set-up based on an AFM and a PFM) in a Multimode Scanning Probe Microscope with a Nanoscope IV controller (Veeco FPP-100). In our experiments, piezoresponse film images were acquired in ambient air by applying a small *ac* voltage with an amplitude of 2.5 V (peak to peak) and a frequency of 10 kHz while scanning the film surface. To apply the external voltage, a standard gold-coated Si_3N_4 cantilever with a spring constant of 0.09 N/m. The probing tip with an apex radius of about 20 nm was in mechanical contact with the uncoated film surface during the measurements. Cantilever vibration was detected using a conventional lock-in technique. From these measurements, the strain profile was determined.

3. Results and discussion

3.1. X-ray diffraction and Rietveld refinement analysis

Fig. 1(a) shows the XRD patterns and (b) Rietveld refinement plot of BNFO thin films heat-treated at 500 °C in static air for 2 h.

In Fig. 1(a), the XRD patterns indicate that BNFO thin films present a tetragonal structure with a space group P4*mm* (No. 99) which is in agreement with the results of Yun et al. [52] and the literature [53–55]. Diffraction peaks related to the deleterious phase ($Bi_2Fe_4O_9$ and $Bi_{46}Fe_2O_{72}$) were not detected, indicating a monophasic system. Moreover, sharp and well-defined diffraction peaks indicate that this film material has a good degree of structural order or periodicity at long range. Fig. 1(a) exhibits small shoulders in the XRD peaks which are related to tetragonal structure.

To verify and confirm if the structure of BNFO thin films is tetragonal it was performed a structural refinement by the Rietveld method. The Rietveld method is a least squares refinement procedure where the experimental step-scanned values are adapted to calculated ones. The profiles are considered to be known, and a model for a crystal structure available [56]. This structural refinement method presents several advantages over conventional

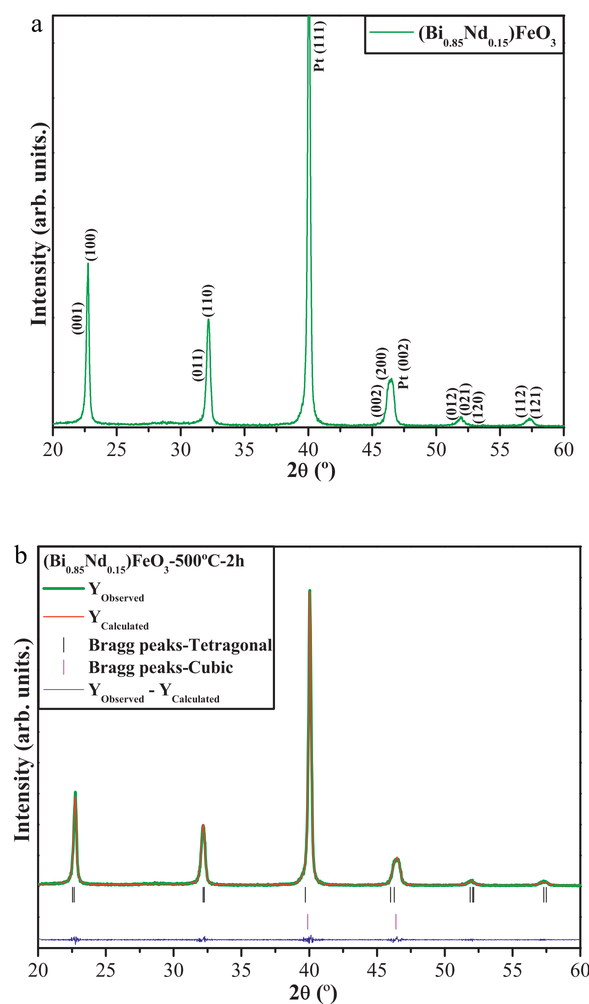

Fig. 1. (a) XRD patterns and (b) Rietveld refinement plot of BNFO thin films heat-treated at 500 °C for 2 h in static air. The vertical line in black color is related to Bragg peaks with tetragonal structure and in pink color is related to Bragg peaks with cubic structure.

quantitative analysis methods. As the method uses a whole pattern-fitting algorithm, all lines for each phase are explicitly considered, and even severely overlapped lines are usually not a problem. Thus, it is not necessary to decompose patterns into separate Bragg peaks, as is often the case for traditional methods. The use of all reflections in a pattern rather than just the strongest ones minimizes both the uncertainty in the derived weight fractions and the effects of preferred orientation, primary extinction, and nonlinear detection systems [57].

The structural refinement was performed in Maud program [58], employing the Rietveld texture and stress analysis [59]. According to the literature [60], the quality of the data from structural refinement is generally checked by *R*-values (R_{wnb}, R_b, R_{exp}, R_w and σ). Since, that the numbers obtained for *R*-values and σ are easy to communicate and with good consistency to tetragonal structure of the BNFO thin films. However, the difference between the plot observed and calculated patterns still is the best way to judge the success of a Rietveld refinement. We have obtained and selected the *R*-values that are given by the following equations [60,61]:

$$R_{wnb} = \frac{\sum |(I_k(observed))^{1/2} - (I_k(calculated))^{1/2}|}{\sum (I_k(observed))^{1/2}} \quad (1)$$

$$R_b = \frac{\sum |(I_k(observed)) - (I_k(calculated))|}{\sum (I_k(observed))} \quad (2)$$

$$R_{\exp} = \frac{\sum |y_i(observed)) - (1/c)y_i(calculated))|}{\sum y_i(observed))} \quad (3)$$

$$R_w = \left[\frac{\sum w_i(y_i(observed)) - (1/c)y_i(calculated)^2)}{\sum w_i(y_i(observed))^2} \right]^{1/2} \quad (4)$$

$$\sigma = \frac{R_w}{R_{\exp}} \quad (5)$$

where y_i is the the measured (and calculated) intensities at each step, or channel, in the energy dispersive mode. The summation index i is running over all points in the diffraction pattern, or in some routines running over the section of the pattern selected for fitting and w_i is data equal a $1/(\sqrt{I_i^{\exp}})$.

Moreover, other parameters and additional functions were applied to find a structural refinement with better quality and reliability. The optimized parameters were scale factor, background with exponential shift, exponential thermal shift and polynomial coefficients, basic phase, microstructure, crystal structure, size-strain (anisotropic no rules), structure solution model (genetic algorithm SDPD), shift lattice constants, profile half-width parameters (u, v, w), texture [62–64], lattice parameters (a, b, c), factor occupancy, atomic site occupancies (Wyckoff). The Rietveld refinement for BNFO thin films was performed based on the BNFO phase with perovskite-type tetragonal structure with a better approximation and indexing with the Crystallographic Information File (CIF) (see Supplementary data-SD1) and with the CIF No. 64917 referent to platinum substrate (cubic structure) [65].

The quality of structural refinement also can be verified by the value of R_w factor, that is very important. Its absolute value does not depend on the absolute value of the intensities, but it depends on the background. With a high background is more easy to reach very low values. Increasing the number of peaks (sharp peaks) is more difficult to get a good value. The structural refinement data are acceptable, when the R_w < 10% for a medium complex phase, for a high complex phases (monoclinic to triclinic) a value of R_w < 15% and for a highly symmetric material or compound (cubic) with few peaks a value of R_w < 8% [66]. Finally, is very important verified the σ values. A good refinement gives σ values lower than 2. However, in the experimental XRD patterns with very high intensities and low noise is difficult to reach a value of 2. As it can be observed in Fig. 1(b), a good agreement between the observed XRD patterns and theoretical results can be noted indicating the success of Rietveld refinement method. The obtained results from the structural refinement are displayed in Table 1.

In this table, the fitting parameters (R_{wnb}, R_b, R_{exp}, R_w and σ) indicate a good agreement between the refined and observed XRD patterns for the BNFO thin films with a tetragonal structure. The small variations in the lattice parameters, unit cell volumes and displacements on Fe atoms (network formers) are indicative of distortions/strain into the lattice caused by differences in the crystal lattice parameters and the thermal expansion behavior between the BNFO film and the underlying substrate or arising from defects promoted by $[BiO_{12}]$ and $[NdO_{12}]$ clusters (network modifiers).

Table 1
Rietveld refinement results and atomic coordinates employed to model the BNFO supercells.

Atoms	Wyckoff	Site	x	y	z
Bismuth	1a	4 mm	0	0	0
Neodymium	1b	4 mm	0	0	0
Iron	1d	4 mm	0.5	0.5	0.51226
Oxygen 1	1b	4 mm	0.5	0.5	−0.0224
Oxygen 2	2c	2 mm	0	0.5	0.48979

$a = b = 3.9042(4)$ Å, $c = 3.9503(0)$ Å, $c/a = 1.0118$, $V = 60.21(1)$ Å^3, space group = P4mm, No. 99.
R_w = 9.7866%; R_{wnb} = 7.8866%; R_b = 6.0232%; R_{exp} = 4.8884% and σ = 2.002.
Weights of the phases in the thin films: $(Bi_{0.85}Nd_{0.15})FeO_3$ = 25.35% and Pt(1 1 1) = 74.65%.

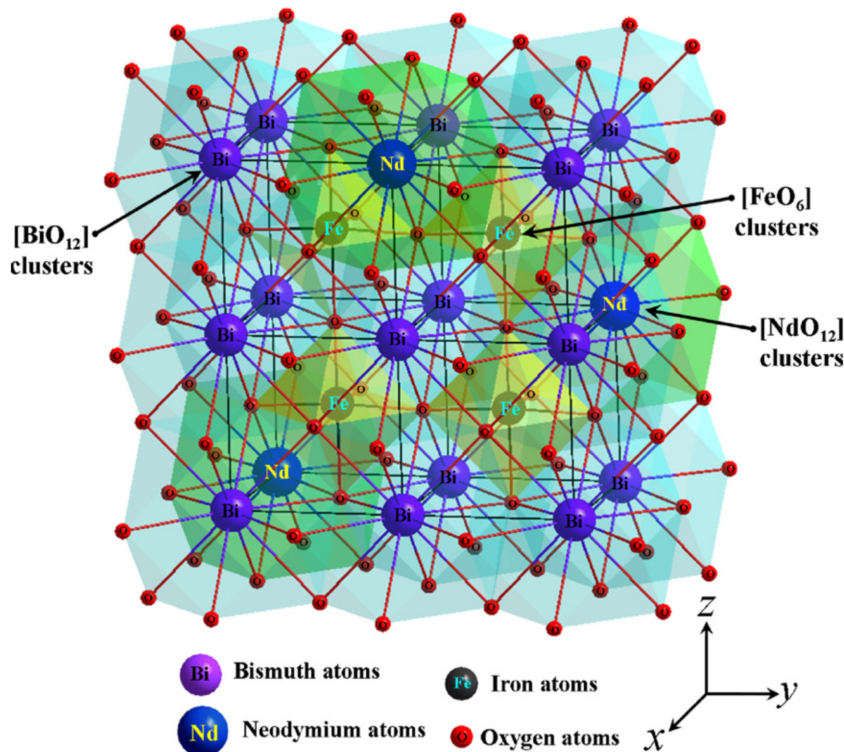

Fig. 2. Schematic representation of crystalline BNFO supercells (1 × 2 × 2) with three type of clusters: $[FeO_6]$, $[BiO_{12}]$ and $[NdO_{12}]$.

3.2. Superstructures with distorted clusters for the BNFO supercells

Fig. 2 illustrates the schematic representation for a tetragonal BNFO supercells (1 × 2 × 2) performed from the Rietveld refinement data.

This supercells were modeled through Diamond Crystal and Molecular Structure Visualization (Version 3.2f for Windows) software [67], using the atomic coordinates presented in Table 1. In this supercells, the Fe atoms (lattice formers) are coordinated to six O atoms in an octahedral configuration and symmetry (O_h) forming the distorted [FeO_6] clusters (Fig. 2) [68]. In this tetragonal supercells, the Fe atoms are slightly displaced along the [0 0 1] direction (z-axis). This behavior can be probably influenced by the neighboring [BiO_{12}] and [NdO_{12}] clusters that are interconnected as verified by the Rietveld refinement data listed in Table 1. While, the Bi and Nd atoms (lattice modifiers) are coordinated to 12 O-atoms in a cuboctahedral configuration and symmetry (O_h) forming the [BiO_{12}] and [NdO_{12}] clusters (Fig. 2) [68]. We believe that the good index for tetragonal structure in BNFO thin films can be a consequence of smaller difference between the ionic radii of Nd^{3+} (1.109 Å) in relation to ionic radii of Bi^{3+} (1.17 Å) [69].

3.3. FE-SEM analyses

Fig. 3(a) and (b) shows the FE-SEM micrographs of the surface microstructure and cross-section of BNFO thin films heat-treated at 500 °C for 2 h in static air, respectively.

As it can be seen in Fig. 3(a), grain growth occurs by the reduction in the total grain boundary area and favors the junction between grains, resulting in the formation of necks [70]. Moreover, the surface is compact and smooth. Also, some elongated grains associated with the high crystallization rate of BNFO thin films was noted. The grain growth process and film densification is characterized by a pore volume elimination related to a mass transport mechanism by grain diffusion with low energy in the grain boundary [71]. Fig. 3(b) shows the presence of a good film/substrate interface obtained by heat treatment at 500 °C for 2 h in static air and an average thickness (t) of about 520 nm.

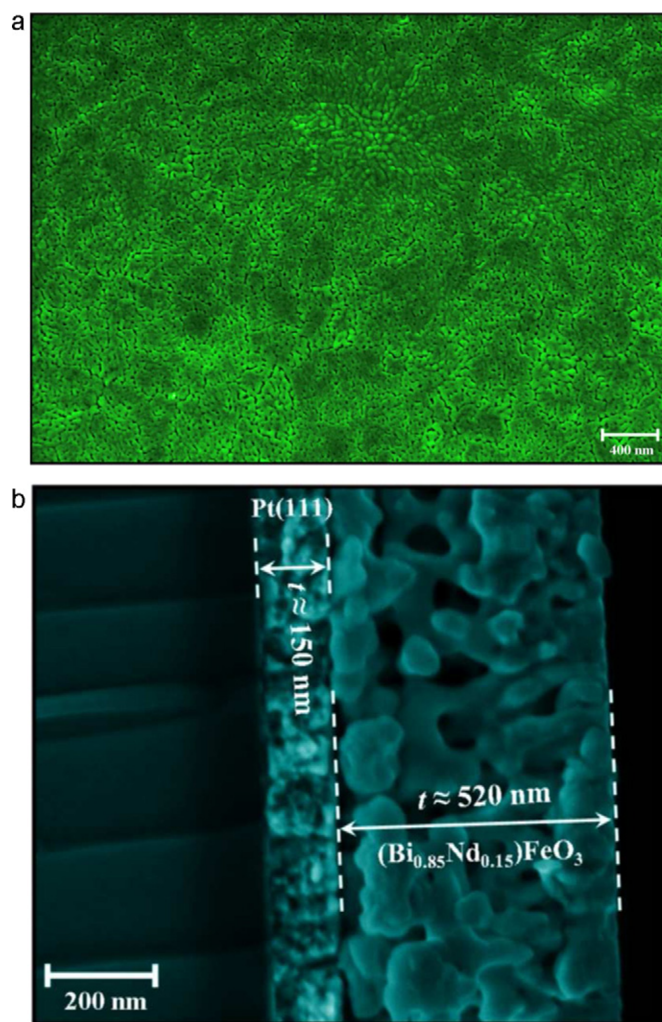

Fig. 3. FE-SEM micrographs of BNFO thin films deposited on Pt substrates heat-treated at 500 °C for 2 h in static air: (a) surface; and (b) cross section.

3.4. AFM and PFM analyses

Fig. 4(a)–(c) illustrates the AFM topography micrographies: (a), PFM micrographs (b) out-of-plane and (c) in-plane of BNFO thin films heat-treated at 500 °C for 2 h in static air.

The piezoelectric effect is a direct manifestation of the presence of polarization. Therefore, PFM micrographs are an indispensable tool to understand the polarization distribution within domains at nanoscale [72]. Also, the PFM micrographs have been employed in this paper to investigate the ferroelectric domain structure and domain dynamics in [0 0 1] oriented BNFO thin films. Fig. 4(a) shows the AFM topography micrograph illustrating the presence of grains with two stable states: bright plateaus that we interpret to arise from the tetragonal phase, and areas of dark contrast that we interpret to arise from the rhombohedral phase. Thus, the PFM micrographies indicate the existence of some nanodomains with rhombohedral phase (white contrast) involved in a matrix formed globally by tetragonal structure. These results are in agreement with recent papers reported in the literature [73,74]. Fig. 4(b) shows a PFM micrograph which corresponds to out-of-plane (OP) with the switching of the polarization upon application of an electric field. The grains which exhibit no contrast change are associated with zero out-of-plane polarization. A similar situation was observed when a positive bias was applied to the film [73,74]. We noticed that some of the grains exhibit a white contrast associated with a component of the polarization pointing toward the bottom electrode. On the other hand, in the in-plane PFM images (Fig. 4(c)), the contrast changes were associated with changes in the in-plane polarization components. In this case, the white contrast indicates polarization (for example, in the positive direction of the z-axis) while the dark contrast shows in-plane polarization components pointing to the negative part of the y-axis. In this case, two types of domain behavior in 71° and 180° domain switchings are characteristic of the rhombohedral phase, but the uniform image contrast in PFM micrographs suggests a striped-domain pattern oriented at 45° which is related to the tetragonal phase [75–77].

3.5. Strain behavior analysis

Fig. 5 illustrates electric field induced changes in surface displacement which are represented as strains of BNFO thin films heat-treated at 500 °C for 2 h in static air.

The unipolar strain exhibits a classic "butterfly" loop structure and presents a maximum at 5 kV/cm while the saturation regime is reached at 10 kV/cm. The [NdO_{12}] clusters in the lattice affect the strain behavior, in part due to domain reorientation [78] (Fig. 5). Beyond that point, it is possible that a moderate bias field results in the transition from an asymmetric phase to a symmetric phase. This field-induced phase transition may be ascribed to the pinch-

Fig. 4. AFM and PFM micrographs of BNFO thin films heat-treated at 500 °C for 2 h in static air: (a) AFM micrograph topography of surface, PFM micrographs (b) out-of-plane of surface and (b) in-plane of surface.

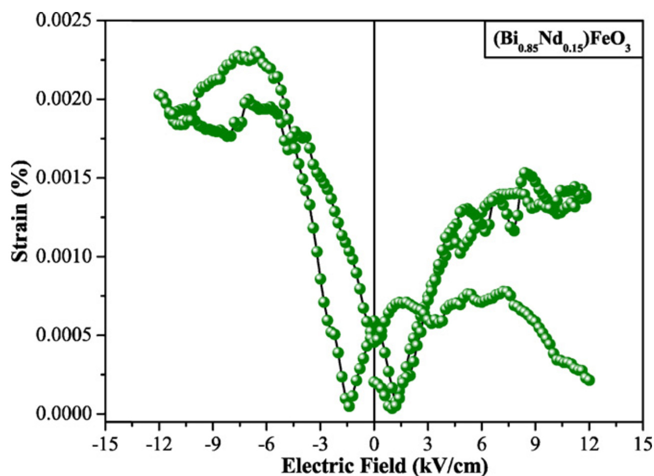

Fig. 5. Strain response of BNFO thin films heat-treated at 500 °C for 2 h in static air.

ing effect; i.e., the consequent decrease in free energy difference among polymorphic phases [78]. A careful inspection of the *S*–*E* plots reveals that there are two apparent linear regions at low fields ($E < 5$ /cm) and high fields ($E > 10$ kV/cm) and one transition region that corresponds to a domain reorientation induced by external electric fields. The hysteretic strain could be associated with domain reorientation. The strain is hysteresis-free at electric fields higher than 5 kV/cm, indicating a stable single domain/poling state induced by the high external electric fields [79]. In addition, from the *S* vs *E* profiles, no noticeable induced phase transition is observed at such high electric fields. It is shown that the unipolar strain was ($S = 0.17\%$). The strain response can be associated with the reduced polarizability and the pinning effect caused by the addition of neodymium [80]. As can be seen, the small strain variations on each curve with an electric field can probably be caused by a clamping effect due to the stress created in the film–substrate interface and the existence of an ultrathin air gap between the tip and the sample which might lower the actual voltage drop in the film.

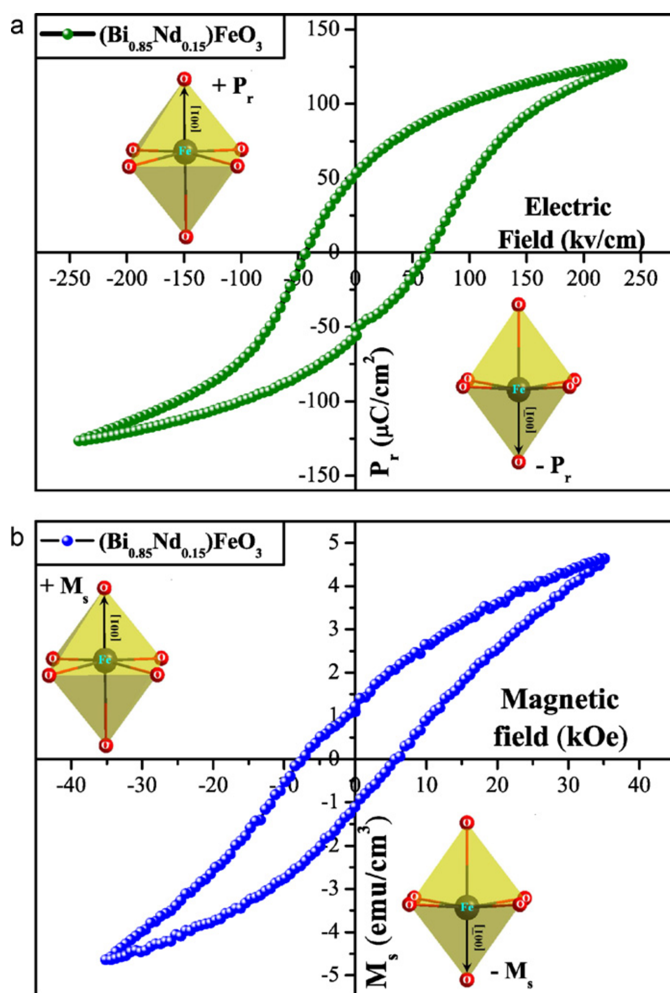

Fig. 6. Ferroelectric properties of BNFO thin films heat-treated at 500 °C for 2 h in static air: (a) *P*–*E* hysteresis loops and (b) *M*–*H* hysteresis loops.

3.6. Ferroelectric and magnetic properties analyses

Fig. 6(a) and (b) illustrates the ferroelectric (*P*–*E*) and magnetic (*M*–*H*) hysteresis loops which explain the ferroelectric and magnetic properties of BNFO thin films heat-treated at 500 °C for 2 h in static air, respectively.

The *P*–*E* hysteresis loop is well saturated and rectangular with a remnant polarization (P_r) of 54 μC/cm^2 under an applied field of 230 kV/cm (Fig. 6(a)). During the hysteresis loop measurement, no sign of leakage was observed under such a measuring frequency. Liu et al. [81] have reported a low P_r for $BiFeO_3$ thin films doped with Ti. This behavior may be attributed unsaturated polarization. In research reported recently, Hu et al. [82] showed an enhancement of the multiferroic properties of $BiFeO_3$ thin films by Nd and high-valence Mo co-doping (BNFM film) which exhibited a well-saturated P_r of 43 μC/cm^2. Also, Singh and Ishiwara [83] related an improvement in the electrical properties of $BiFeO_3$ thin films doped with La and a significant P_r of 52 μC/cm^2. In the research of these authors, the P_r is lower than our results, probably due to the displacement of [FeO_6] octahedron clusters along the [1 1 1] direction (rhombohedral) and projection polarization along different orientations in the [0 0 1] direction (tetragonal) with a larger polarization (inset Fig. 6(a)). Jang et al. [84] found that (0 0 1)-oriented films exhibit a strong strain tunability of their out-of-plane remanent polarization, indicating that the strain induced rotation mechanism of the spontaneous polarization direction. *M*–*H* hysteresis loops were recorded at 300 K (Fig. 6(b)). The saturation magnetization (M_s) for the BNFO thin film was 1.3 emu/cm^3. A weak ferromagnetic response was noted for BNFO thin films due to Nd^{3+} substitution for the volatile Bi^{3+} which causes a reduction in Fe^{2+} valence states and induces a low value for M_s as reported and investigated by X-ray photoelectron spectroscopy (see Refs. [52,82]). Therefore, the substitution of Fe^{3+} ions with higher valence requires a charge compensation for its electric neutrality. In our work, we suggested a larger distribution of iron ions with valence (+3) states in [FeO_6] clusters into the BNFO lattice, leading to weak ferromagnetism (inset Fig. 6(b)). Also, the presence of weak ferromagnetism in the BNFO thin film may be attributed to either the canting of the antiferromagnetically ordered spins by a structural distortion [85–87] or the breakdown of the balance between the antiparallel sublattice magnetization of Fe^{3+} ions due to metal ion substitution with a different electron densities [88]. As can be seen in Fig. 6(b), the magnetization of our film linearly increases with the applied magnetic field. However, further studies are required to understand the magnetic behavior of BNFO thin film. The low coercive magnetic fields of BNFO thin films are indicative of their magnetically soft nature and device application suitability.

Fig. 7(a) and (b) illustrates the magnetoelectric coefficient vs the *dc* bias magnetic field in the longitudinal and transversal directions. The curve presents hysteretic behavior as observed in the magnetic field cycles for BNFO thin films heat-treated at 500 °C for 2 h in static air, respectively.

As shown in Fig. 7(a), BNFO thin films have a maximum magnetoelectric coefficient (α_{ME}) longitudinal of about 12 V/cm Oe. This longitudinal direction is much larger than the results recently reported [89–91] for $BiFeO_3$ ceramics with doping (Sr, Ba, La, Nd) (as high as 2.3 and 6.3 V/cm Oe at zero fields). This behavior is related to the antiferromagnetic *z*-axis of BNFO thin films with a predominant tetragonal structure due to the splitting of magnetic diffraction maxima which can be interpreted in terms of a magnetic cycloidal spiral with a long period 620 ± 20 Å [92]. Fig. 7(b) shows that a maximum α_{ME} transversal of about 3 V/cm Oe at zero field for our BNFO thin films which are very close to the literature value for $BiFeO_3$ multiferroic thin film heterostructures [79]. Moreover, other researchers reported that a necessary condition to observe a linear magnetoelectric effect and spontaneous magnetization in $BiFeO_3$ materials is that the spatially modulated spin structure be destroyed [93]. Significant magnetization (≈0.5 μB/unit cell) and a strong magnetoelectric coupling have been observed in epitaxial thin films, suggesting that the magnetic moments of iron ions, preserving a locally antiparallel orientation can be are turned in a spiral-oriented direction and could be suppressed in BNFO thin films [94].

Fig. 8(a) and (b) illustrates the complex impedance and capacitive measurements for BNFO thin films heat-treated at 500 °C for 2 h in static air, respectively.

The feature at the highest measuring frequency is characteristic of the *R*–*L* resonance form as well as the measuring leads and electrode itself. On the other hand, the region of lower frequencies shows an inverse behavior as can be observed by complex impedance (Fig. 8(a)). This range accounts for grain–grain junctions and controls the global conductivity response as it is strongly related to the dielectric mechanism [95]. Moreover, the complex capacitive diagram indicates that the capacitance of the electrodes is only slightly affected by the structure of the ferroelectric material. With regard to the reduction of dielectric properties above 10^7 Hz, it can be inferred that the number of active internal domains is minimized at such high frequency, particularly the grain's internal domain. The chemistry of dielectric internal domains most likely depends on the neodymium amount to increase its effectiveness. Fig. 8(b) illustrates the effects of the interface on the capacitance

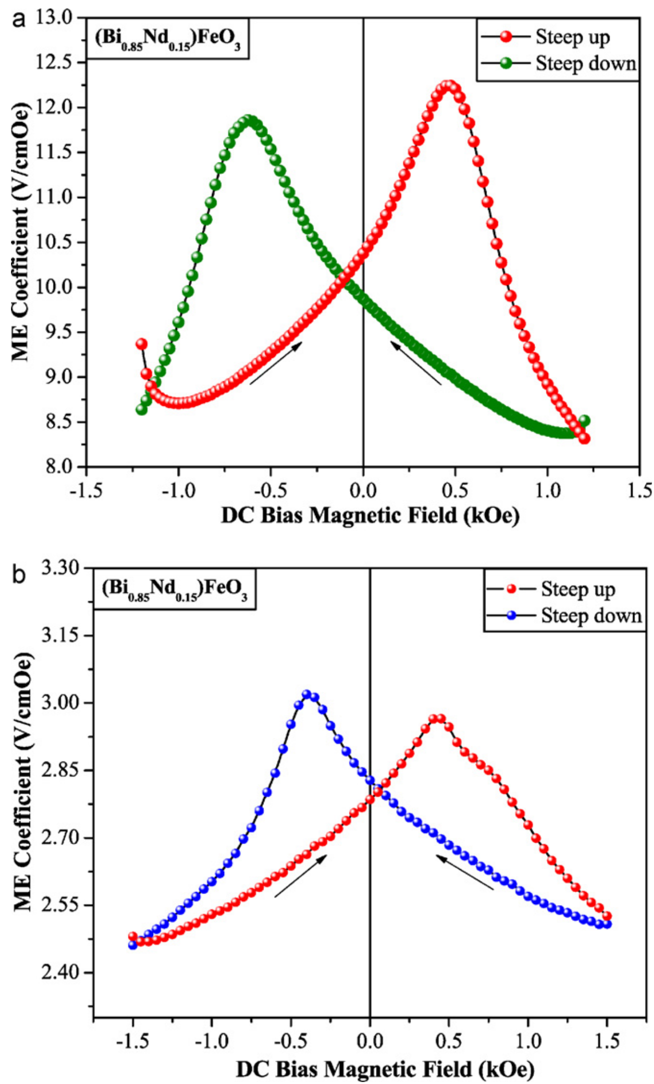

Fig. 7. *M–E* curve coefficient dependence on *dc* bias magnetic field of BNFO thin films heat-treated at 500 °C in static air for 2 h in 7 kHz *ac* magnetic field at room temperature: (a) longitudinal and (b) transversal.

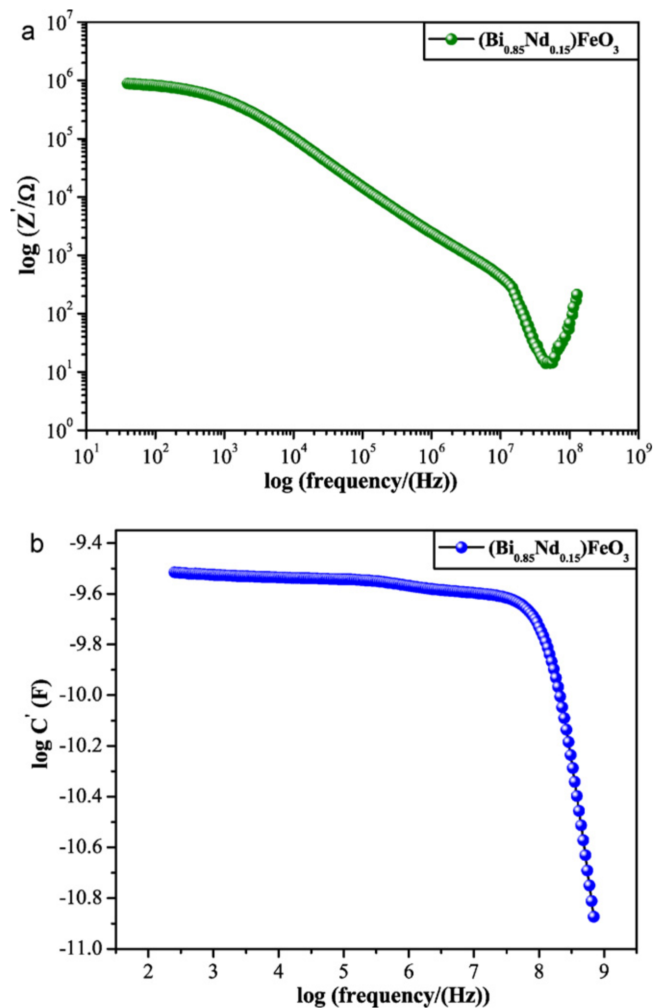

Fig. 8. (a) Bode capacitive diagrams and (b) logarithm of the real part of the complex capacitance as a function of frequency of BNFO thin films heat-treated at 500 °C for 2 h in static air.

from intermediate to low frequencies. Such a relaxation pattern can be described by an equivalent circuit consistent with three parallel contributions: (I) the high frequency limit related to grain boundary capacitances; (II) the complex incremental capacitance at intermediate frequencies related to the relaxation of the particular structure found in the space charge region; and finally (III) in the low frequency region, the term representing the *dc* conductance of the multi-junction device. The high frequency region of the complex capacitance diagrams shows the presence of a dipolar relaxation process possessing a near-Debye pattern. It is important to emphasize here that, in the present discussion, because the dielectric properties may be strongly related to the a multi-junction domain [96,97], it is inappropriate to use parameters such as dielectric permittivity or susceptibility since it is almost impossible to have sufficient knowledge about the geometry (i.e., the thickness of the region in question [domain boundaries existing in the grain]) to determine the complex permittivity. Thus we prefer to express the response in terms of complex capacitance (C^*) instead of complex dielectric form (ε^*) [98]. Responses to sample–electrode interfaces are evident and appear at the lowest measuring frequencies. These sample–electrode interfaces have very high polarization (due to the thin film geometry of the interface) and high charge density (due to any space charge effects). For practical applications, the films are preferred to be less conductive. As previously verified in our early research [99], the oxygen vacancy concentration is affected by the annealing atmosphere. The thermal treatment in an oxidant atmosphere in materials with *p*-type conductivity increases the defects as Bi or Fe vacancies, resulting in an increase in conductivity with increasing oxygen content, indicating that the mobile carriers are positively charged and that the possibility of hopping through the Bi^{3+} ion can be considered. Taking into account that we have annealed the BNFO thin film in static air, the oxygen vacancies are ordered, avoiding polarization and therefore reducing conductivity. Thus, fewer possibilities for the electron trapping results in a highly resistance film.

3.7. Leakage current density analyses

Fig. 9(a) and (b) illustrates the bias curve of the leakage current density log(*J*) as a function of the applied electric field and the *J–E* curve leakage current density as a function of an applied electric field in a logarithmic scale for BNFO thin films heat-treated at 500 °C for 2 h in static air, respectively.

Fig. 9(a) shows the measurement bias curve of the leakage current density log(*J*) vs the electric field (*E*) plot for a BNFO thin film. The measured low leakage current densities confirmed that the BNFO thin film had high resistivity. Even at high positive and nega-

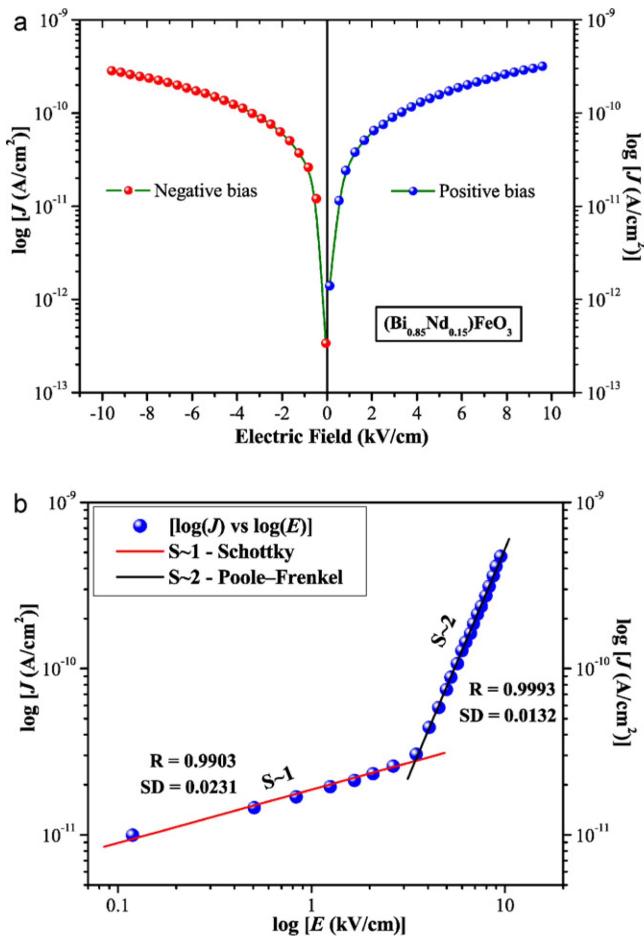

Fig. 9. (a) Log$J$–E bias curve of the leakage current density as a function of the applied electric field and (b) log$J$–log$E$ curve leakage current density as a function of an applied electric field for the BNFO thin films heat-treated at 500 °C for 2 h in static air.

tive applied electric fields of 10 kV/cm, the leakage current densities were both 1.5×10^{-10} A/cm^2 which were quite reasonable, considering recent publications for BNFO thin films reported in the literature [100,101]. There are many possible mechanisms to deal with the leakage current limiting mechanisms for BNFO thin films in Fig. 9(a). These mechanisms are concentrated in two categories: (I) interface-limited conduction mechanisms; and (II) bulk limited conduction mechanisms. The leakage current density increases linearly with the external electric field in the low electric field region, suggesting an ohmic conductor which characteristic of the Schottky emission as a first mechanism [102]. This first mechanism is the interface-limited Schottky emission which arises from a difference in Fermi levels between a metal (Pt-electrode) and an insulator or semiconductor (BNFO film). The energy difference creates a potential barrier between the metal and the insulator that charges must overcome [103]. The current density across a Schottky barrier is described by the equation below:

$$J_S = A^* T^2 \ \exp\left(\frac{\beta E^{1/2} - \phi_B}{k_B T}\right) \tag{6}$$

The term B is defined below:

$$B = \left(\frac{q^3}{4\pi\varepsilon_0\varepsilon_r}\right)^{1/2} \tag{7}$$

where A^* is the effective Richardson constant, k_B is the Boltzmann constant, T is the temperature, E is an applied electric field, ϕ_B is the Schottky barrier height, ε_0 is the permittivity of free space, ε_r is the relative dielectric constant of the ferroelectric material, and q is the electron charge, respectively. The second mechanism considered is the bulk-limited space-charge-limited conduction (SCLC). The limitation arises from a current impeding space charge which forms as charges are injected into the film from the electrode at a rate faster than they can travel through the BNFO film. The current density for SCLC is described by the equation below:

$$J_{\mathrm{SCLC}} = \frac{9\mu\varepsilon_0\varepsilon_r V^2}{8t^3} \tag{8}$$

where μ is the carrier mobility and t is the thin film thickness. The third mechanism is the bulk-limited Poole–Frenkel emission. This conduction mechanism involves the consecutive hopping of charges between defect trap centers [104]. The ionization of the trap charges can be both thermally and field activated. The conductivity for the Poole–Frenkel emission is described by the equation below:

$$\sigma_{\mathrm{FP}} = c \ \exp - \left[\frac{E_1}{k_B T} - \frac{1}{k_B T}\left(\frac{q^3 V}{\pi\varepsilon_0\varepsilon_r t}\right)^{1/2}\right] \tag{9}$$

where c is a constant and E_1 is the trap ionization energy.

To confirm the conduction mechanism of the BNFO thin film, the leakage current density as a function of an applied electric field in a logarithmic scale [log(J) vs log(E)] was plotted as shown in Fig. 9(b). The plot can be fitted well by linear segments with different slopes. At a low electric field regime, the slope is close to 1 ($S \sim 1$), indicating a linear Ohmic conduction which is dominated by thermally stimulated free electrons. The leakage current for Ohmic conduction can be expressed by the equation below:

$$J = q\mu NeE \tag{10}$$

where Ne is the density of the thermally stimulated electrons. With an increasing applied field, electrons will be injected into the insulator. At a sufficiently high applied electric field regime, the density of free electrons due to carrier injection becomes greater than the density of thermally stimulated free electrons. Then the current density follows the SCL current law [105]. The change of the slope to 2 ($S \sim 2$) indicates a transition of the conduction mechanism from Ohmic to SCLC with increasing electric field strength. Therefore, we believe that the origin of reduced leakage current in the BNFO thin film can be related to several effects, such as: no presence of deleterious phases in the lattice, reduction of oxygen vacancies, stabilization of oxidation state (Fe^{3+}) and smooth surface microstructure with dense grains due to incorporation of Nd modifier in Bi site.

4. Conclusions

In summary, we have obtained BNFO thin films on the Pt(1 1 1)/Ti/SiO_2/Si substrates by the polymeric precursor method after heat treatment at 500 °C for 2 h in static air. XRD patterns and Rietveld refinements analysis confirmed that BNFO thin films present a tetragonal structure at long range. FE-SEM micrographs showed that BNFO thin films present a homogeneous, smooth surface without cracks and with an average thickness of about 520 nm. AFM and PFM micrographs exhibited the presence of grains with two stable states: bright plateaus to the tetragonal phase and dark contrasts to the rhombohedral phase. Moreover, these micrographs reveal the possible co-existence of the tetragonal and rhombohedral phases in nanodomains of BNFO thin films. Two types of nanodomain behavior in 71° and 180° for the main domain switchings are characteristic of the rhombohedral phase, but a uniform image contrast in the PFM micrographs suggests a striped-domain pattern oriented at 45° which is related to the tetragonal

phase. A unipolar strain response with (S = 0.17%) can be associated with the reduced polarizability and the pinning effect caused by the addition of neodymium into the lattice. Ferroelectric and magnetoelectric properties are evidenced by hysteresis loops. The maximum magnetoelectric coefficient in the longitudinal direction was close to 12 V/cm Oe. The leakage current density at 5.0 V is equal to 1.5×10^{-10} A/cm^2 with two main dominant mechanisms in the low-leakage current (Schottky and Poole–Frenkel). Finally, the Nd modifier was found to effectively induce spontaneous magnetization in antiferromagnetic $BiFeO_3$, thus exhibiting good ferroelectric/magnetoelectric properties and leakage current density due to reduction of oxygen vacancies, stabilization of oxidation state (Fe^{3+}) and smooth surface microstructure with dense grains.

Acknowledgements

The authors thank the financial support of the Brazilian Research Financing Institutions: FAPESP-Postdoctorate (No. 2009/50303-4), CNPq and CAPES.

Appendix A. Supplementary data

Supplementary data associated with this article can be found, in the online version, at doi:10.1016/j.jallcom.2011.02.030.

References

[1] T. Zhao, A. Scholl, F. Zavaliche, K. Lee, M. Barry, A. Doran, M.P. Cruz, Y.H. Chu, C. Ederer, N.A. Spaldin, R.R. Das, D.M. Kim, S.H. Baek, C.B. Eom, R. Ramesh, Nat. Mater. 5 (2006) 823–829.
[2] S. Shastry, G. Srinivasan, M.I. Bichurin, V.M. Petrov, A.S. Tatarenko, Phys. Rev. B 70 (2004) 064416–064421.
[3] H. Zheng, J. Wang, S.E. Lofland, Z. Ma, L. Mohaddes-Ardabili, T. Zhao, L. Salamanca-Riba, S.R. Shinde, S.B. Ogale, F. Bai, D. Viehland, Y. Jia, D.G. Schlom, M. Wuttig, A. Roytburd, R. Ramesh, Science 303 (2004) 661–663.
[4] N.A. Hill, J. Phys. Chem. B 104 (2000) 6694–6709.
[5] H. Yang, H. Wang, G.F. Zou, M. Jain, N.A. Suvorova, D.M. Feldmann, P.C. Dowden, R.F. DePaula, J.L. MacManus-Driscoll, A.J. Taylor, Q.X. Jia, Appl. Phys. Lett. 93 (2008) 142904–142906.
[6] M. Popa, S. Preda, V. Fruth, K. Sedlácková, C. Balázsi, D. Crespo, J.M. Calderón-Moreno, Thin Solid Films 517 (2009) 2581–2585.
[7] S. Mukherjee, R. Gupta, A. Garg, V. Bansal, S. Bhargava, J. Appl. Phys. 107 (2010) 123535–123537.
[8] S. Das, S. Basu, S. Mitra, D. Chakravorty, B.N. Mondal, Thin Solid Films 518 (2010) 4071–4075.
[9] X. Tang, J. Dai, X. Zhu, H. Lei, L. Yin, W. Song, Y. Cheng, D. Wu, Y. Sun, J. Magn. Magn. Mater. 322 (2010) 2647–2652.
[10] Z. Wen, G. Hu, S. Fan, C. Yang, W. Wu, Y. Zhou, X. Chen, S. Cui, Thin Solid Films 517 (2010) 4497–4501.
[11] J.H. Xu, H. Ke, D.C. Jia, W. Wang, Y. Zhou, J. Alloys Compd. 472 (2009) 473–477.
[12] H. Liu, X. Wang, J. Sol–Gel Sci. Technol. 47 (2008) 154–157.
[13] S.V. Kiselev, R.P. Ozerov, G.S. Zhdanov, Sov. Phys. Dokl. 7 (1963) 742–744.
[14] J.R. Teague, R. Gerson, W.J. James, Solid State Commun. 8 (1970) 1073–1074.
[15] F. Kubel, H. Schimid, Acta Crystallogr. B 46 (1990) 698–702.
[16] P. Fischer, M. Polomska, M. Szymanski, J. Phys. Solid State Phys. 13 (1980) 1931–1940.
[17] C. Michel, J.M. Moreau, G.D. Achenbach, R. Gerson, W.J. James, Solid State Commun. 7 (1969) 701–704.
[18] R. Ramesh, N.A. Spaldin, Nat. Mater. 6 (2007) 21–29.
[19] S.K. Pradhan, J. Das, P.P. Rout, S.K. Das, S. Samantray, D.K. Mishra, D.R. Sahu, A.K. Pradhan, K. Zhang, V.V. Srinivasu, B.K. Roul, J. Alloys Compd. 509 (2011) 2645–2649.
[20] A. Huang, S.R. Shannigrahi, J. Alloys Compd. 509 (2011) 2054–2059.
[21] X. Zhang, Y. Sui, X. Wang, Y. Wang, Z. Wang, J. Alloys Compd. 507 (2010) 157–161.
[22] V. Shelke, V.N. Harshan, S. Kotru, A. Gupta, J. Appl. Phys. 106 (2009) 104114–1041120.
[23] T. Kawae, Y. Terauchi, H. Tsuda, M. Kumeda, A. Morimoto, Appl. Phys. Lett. 94 (2009) 112904–112906.
[24] Z. Wen, X. Shen, J. Wu, D. Wu, A. Li, B. Yang, Z. Wang, H. Chen, J. Wang, Appl. Phys. Lett. 96 (2010) 202904–202906.
[25] A.Z. Simões, L.S. Cavalcante, C.S. Riccardi, J.A. Varela, E. Longo, Curr. Appl. Phys. 9 (2009) 520–523.
[26] J. Yan, G.D. Hu, X.M. Chen, W.B. Wu, C.H. Yang, J. Appl. Phys. 104 (2008) 076103–1041120.
[27] V.R. Singh, A. Garg, D.C. Agrawal, Solid State Commun. 149 (2009) 734–737.
[28] Y. Du, Z.X. Cheng, M. Shahbazi, E.W. Collings, S.X. Dou, X.L. Wang, J. Alloys Compd. 490 (2010) 637–641.
[29] F. Yan, T.J. Zhu, M.O. Lai, L. Lu, Scripta Mater. 63 (2010) 780–783.
[30] B. Yu, M. Li, Z. Hu, L. Pei, D. Guo, X. Zhao, S. Dong, J. Appl. Phys. 93 (2008) 182909–182911.
[31] P. Uniyal, K.L. Yadav, J. Phys.: Condens. Matter 21 (2009) 405901–405906.
[32] C.J. Cheng, A.Y. Borisevich, D. Kan, I. Takeuchi, V. Nagarajan, Chem. Mater. 22 (2010) 2588–2596.
[33] K.S. Nalwa, A. Garg, A. Upadhyaya, Matter Lett. 62 (2008) 878–881.
[34] K.S. Nalwa, A. Garg, J. Appl. Phys. 103 (2008) 044101–044106.
[35] C.J. Cheng, D. Kan, S.H. Lim, W.R. McKenzie, P.R. Munroe, L.G. Salamanca-Riba, R.L. Withers, I. Takeuchi, V. Nagarajan, Phys. Rev. B 80 (2009) 014109–014119.
[36] H. Liu, T. Liu, X. Wang, Solid State Commun. 149 (2009) 1958–1961.
[37] D. Kothari, V.R. Reddy, A. Gupta, C. Meneghini, G. Aquilanti, J. Phys.: Condens. Matter 22 (2010) 356001–435610.
[38] J. Liu, L. Fang, F. Zheng, S. Ju, M. Shen, Appl. Phys. Lett. 95 (2009) 022511–022513.
[39] V.R. Reddy, D. Kothari, A. Gupta, S.M. Gupta, Appl. Phys. Lett. 94 (2009) 082505–082507.
[40] S.K. Pradhan, J. Das, P.P. Rout, S.K. Das, D.K. Mishra, D.R. Sahu, A.K. Pradhan, V.V. Srinivasu, B.B. Nayak, S. Verma, B.K. Roul, J. Magn. Magn. Mater. 322 (2010) 3614–3622.
[41] C. Fanggao, S. Guilin, F. Kun, Q. Ping, Z. Qijun, J. Rare Earths 24 (2006) 273–276.
[42] F.Z. Qian, J.S. Jiang, S.Z. Guo, D.M. Jiang, W.G. Zhang, J. Appl. Phys. 106 (2009) 084312–184312.
[43] J. Xu, G. Wang, H. Wang, D. Ding, Y. He, Mater. Lett. 63 (2009) 855–857.
[44] J. Wang, M. Li, X. Liu, L. Pei, J. Liu, B. Yu, X. Zhao, Chin. Sci. Bull. 55 (2010) 1594–1597.
[45] B. Vengalis, J. Devenson, A.K. Oginskis, V. Lisauskas, F. Anisimovas, R. Butkute, L. Dapkus, Phys. Status Solidi C 12 (2009) 2746–2749.
[46] F. Huang, X. Lu, Z. Wang, S. Xu, X. Wu, J. Zhu, Integrat. Ferroelect. 96 (2008) 1607–8489.
[47] F. Huang, X. Lu, W. Lin, X. Wu, Y. Kan, J. Zhu, Appl. Phys. Lett. 89 (2006) 242914–242916.
[48] S. Karimi, I.M. Reaney, Y. Han, J. Pokorny, I. Sterianou, J. Mater. Sci. 44 (2009) 5102–5112.
[49] Z.X. Cheng, X.L. Wang, S.X. Dou, H. Kimura, K. Ozawa, J. Appl. Phys. 104 (2008) 116109–116111.
[50] Y.J. Zhang, H.G. Zhang, J.H. Yin, H.W. Zhang, J.L. Chen, W.Q. Wang, G.H. Wu, J. Magn. Magn. Mater. 322 (2010) 2251–2255.
[51] A.H.M. Gonzalez, A.Z. Simões, L.S. Cavalcante, E. Longo, J.A. Varela, C.S. Riccardi, Appl. Phys. Lett. 90 (2007) 052906–052908.
[52] K.Y. Yun, M. Noda, M. Okuyama, H. Saeki, H. Tabata, K. Saito, J. Appl. Phys. 96 (2004) 3399–3403.
[53] Z. Hu, M. Li, Y. Yu, J. Liu, L. Pei, J. Wang, X. Liu, B. Yu, X. Zhao, Solid State Commun. 150 (2010) 1088–1091.
[54] K.Y. Yun, D. Ricinschi, T. Kanashima, M. Okuyama, Appl. Phys. Lett. 89 (2006) 192902–192904.
[55] Z. Cheng, X. Wang, S. Dou, H. Kimura, K. Ozawa, Phys. Rev. B 77 (2008) 092101–092104.
[56] H.M. Rietveld, J. Appl. Cryst. 2 (1969) 65–71.
[57] D.L. Bish, J.E. Post, Am. Mineral. 78 (1993) 932–940.
[58] http://www.ing.unitn.it/maud/index.html.
[59] L. Lutterotti, S. Matthies, H.-R. Wenk, A.J. Schultz, J.J. Richardson, Appl. Phys. 81 (1997) 594–600.
[60] G. Will, Powder Diffraction: the Rietveld Method and the Two Stage Method to Determine and Refine Crystal Structures from Powder Diffraction Data, Springer-Verlag, Berlin, Heidelberg, 2006, pp. 44–69.
[61] S.R. Hall, F.H. Allen, I.D. Brown, Acta Crystallogr. A 47 (1991) 655–685.
[62] M. Ferrari, L. Lutterotti, J. Appl. Phys. 76 (1994) 7246–72556.
[63] L. Lutterotti, M. Bortolotti, IUCr: Compcomm Newslett. 1 (2003) 43–50.
[64] L. Lutterotti, S. Matthies, H.-R. Wenk, IUCr: Newslett. CPD 21 (1999) 14–15.
[65] T. Barth, G. Lundeÿ, Zeitsch. Phys. Chem. 121 (1926) 78–102.
[66] http://ftp.ccp14.dl.ac.uk/ccp/web-mirrors/lutterotti/~luttero/laboratoriomateriali/Rietveld.pdf.
[67] http://www.crystalimpact.com/diamond/Default.htm.
[68] K. Fukushima, M. Kobune, T. Yamaji, H. Tada, A. Mineshige, T. Yazawa, H. Fujisawa, M. Shimizu, Y. Nishihata, J. Mizuki, H. Yamaguchi, K. Honda, Jpn. J. Appl. Phys. 46 (2007) 6938–6943.
[69] R.D. Shannon, Acta Cryst. A 32 (1976) 751–767.
[70] L.S. Cavalcante, J.C. Sczancoski, F.S. De Vicente, M.T. Frabbro, M. Siu Li, J.A. Varela, E. Longo, J. Sol–Gel Sci. Technol. 49 (2009) 35–46.
[71] D. Gouvêa, R.H.R. Castro, Appl. Surf. Sci. 217 (2003) 194–201.
[72] F. Zavaliche, S.Y. Yang, T. Zhao, Y.H. Chu, M.P. Cruz, C.B. Eom, R. Ramesh, Phase Transit. 79 (2006) 991–1017.
[73] A. Kumar, S. Denev, R.J. Zeches, E. Vlahos, N.J. Podraza, A. Melville, D.G. Schlom, R. Ramesh, V. Gopalan, Appl. Phys. Lett. 97 (2010) 112903–112905.
[74] R.J. Zeches, M.D. Rossell, J.X. Zhang, A.J. Hatt, Q. He, C.H. Yang, A. Kumar, C.H. Wang, A. Melville, C. Adamo, G. Sheng, Y.H. Chu, J.F. Ihlefeld, R. Erni, C. Ederer, V. Gopalan, L.Q. Chen, D.G. Schlom, N.A. Spaldin, L.W. Martin, R. Ramesh, Science 326 (2009) 977–980.
[75] Y.H. Chu, Q. He, C.H. Yang, P. Yu, L.W. Martin, P. Shafer, R. Ramesh, Nano Lett. 9 (2009) 1726–1730.
[76] D. Mazumdar, V. Shelke, M. Iliev, S. Jesse, A. Kumar, S.V. Kalinin, A.P. Baddorf, A. Gupta, Nano Lett. 10 (2010) 2555–2561.

[77] D.H. Kim, H.N. Lee, M.D. Biegalski, H.M. Christen, Appl. Phys. Lett. 92 (2008) 012911–012912.
[78] A.Z. Simões, E.C. Aguiar, A.H.M. Gonzalez, J. Andrés, E. Longo, J.A. Varela, J. Appl. Phys. 104 (2008) 104115–104121.
[79] J. Wang, J.B. Neaton, H. Zheng, V. Nagarajan, S.B. Ogale, B. Liu, D. Viehland, V. Vaithyanathan, D.G. Schlom, U.V. Waghmare, N.A. Spaldin, K.M. Rabe, M. Wuttig, R. Ramesh, Science 299 (2003) 1719–1722.
[80] I. Apostolova, J.M. Wesselinowa, J. Magn. Magn. Mater. 321 (2009) 2477–2482.
[81] H. Liu, Z. Liu, K. Yao, J. Sol–Gel Sci. Technol. 41 (2007) 123–128.
[82] Z. Hu, M. Li, B. Yu, L. Pei, J. Liu, J. Wang, X. Zhao, J. Phys. D: Appl. Phys. 42 (2009) 185010–185015.
[83] S.K. Singh, H. Ishiwara, Jpn. J. Appl. Phys. 45 (2006) 3194–3197.
[84] H.W. Jang, S.H. Baek, D. Ortiz, C.M. Folkman, R.R. Das, Y.H. Chu, P. Shafer, J.X. Zhang, S. Choudhury, V. Vaithyanathan, Y.B. Chen, D.A. Felker, M.D. Biegalski, M.S. Rzchowski, X.Q. Pan, D.G. Schlom, L.Q. Chen, R. Ramesh, C.B. Eom, Phys. Rev. Lett. 101 (2008) 107602–1107602.
[85] M. Fiebig, J. Phys. D: Appl. Phys. 38 (2005) R123–R152.
[86] M.M. Kumar, S. Srinath, G.S. Kumar, S.V. Suryanarayana, J. Magn. Magn. Mater. 188 (1998) 203–212.
[87] T. Kanai, S.I. Ohkoshi, A. Nakajima, T. Watanabe, K. Hashimoto, Adv. Mater. 13 (2001) 487–490.
[88] K. Ueda, H. Tabata, T. Kawai, Appl. Phys. Lett. 75 (1999) 555–557.
[89] V.B. Naik, R. Mahendiran, Solid State Commun. 149 (2009) 754–758.
[90] E.V. Ramana, T.B. Sankaram, Mater. Chem. Phys. 120 (2010) 231–235.
[91] A.A. Amirov, I.K. Kamilov, A.B. Batdalov, I.A. Verbenko, O.N. Razumovskaya, L.A. Reznichenko, L.A. Shilkina, Tech. Phys. Lett. 34 (2008) 760–762.
[92] I. Sosnowskat, T. Peterlin-Neumaier, E. Steichele, J. Phys. C: Solid State Phys. 15 (1982) 4835–4846.
[93] A.K. Zvezdin, A.P. Pyatakov, Phys. Usp. 47 (2004) 416–421.
[94] V.M. Mukhortov, Y.I. Golovko, Y.I. Yuzyuk, Phys. Usp. 52 (2009) 856–860.
[95] E. Joanni, R. Savu, P.R. Bueno, E. Longo, J.A. Varela, Appl. Phys. Lett. 92 (2008) 132110–132112.
[96] T.T. Fang, C.P. Liu, Chem. Mater. 17 (2005) 5167–5171.
[97] J. Li, A.W. Sleight, M.A. Subramanian, Solid State Commun. 135 (2005) 260–262.
[98] A.K. Jonscher, Solid State Electron. 33 (1990) 737–742.
[99] A.Z. Simões, C.S. Riccardi, M.L. Dos Santos, F. González Garcia, E. Longo, J.A. Varela, Mater. Res. Bull. 44 (2009) 1747–1752.
[100] H. Uchida, R. Ueno, H. Funakubo, S. Koda, J. Appl. Phys. 100 (2006) 014106–014114.
[101] T. Kawae, H. Tsuda, A. Morimoto, Appl. Phys. Express 1 (2008) 051601–151601.
[102] G.W. Pabst, L.W. Martin, Y.-H. Chu, R. Ramesh, Appl. Phys. Lett. 90 (2007) 072902–072904.
[103] W. Mönch, Phys. Rev. B 37 (1988) 7129–7132.
[104] C. Chaneliere, J.L. Autran, R.A.B. Devine, B. Balland, Mater. Sci. Eng. R 22 (1996) 269–322.
[105] S.W. Yi, S.S. Kim, J.W. Kim, H.K. Jo, D. Do, W.J. Kim, Thin Solid Films 517 (2009) 6737–6741.